

Full-dimensional ground- and excited-state potential energy surfaces and state couplings for photodissociation of thioanisole

Shaohong L. Li and Donald G. Truhlar

Citation: *J. Chem. Phys.* **146**, 064301 (2017); doi: 10.1063/1.4975121

View online: <http://dx.doi.org/10.1063/1.4975121>

View Table of Contents: <http://aip.scitation.org/toc/jcp/146/6>

Published by the [American Institute of Physics](#)



**COMPLETELY
REDESIGNED!**

**PHYSICS
TODAY**

Physics Today Buyer's Guide
Search with a purpose.

Full-dimensional ground- and excited-state potential energy surfaces and state couplings for photodissociation of thioanisole

Shaohong L. Li and Donald G. Truhlar^{a)}

Department of Chemistry, Chemical Theory Center, and Supercomputing Institute, University of Minnesota, Minneapolis, Minnesota 55455, USA

(Received 9 November 2016; accepted 11 January 2017; published online 8 February 2017)

Analytic potential energy surfaces (PESs) and state couplings of the ground and two lowest singlet excited states of thioanisole ($C_6H_5SCH_3$) are constructed in a diabatic representation based on electronic structure calculations including dynamic correlation. They cover all 42 internal degrees of freedom and a wide range of geometries including the Franck-Condon region and the reaction valley along the breaking S-CH₃ bond with the full ranges of the torsion angles. The parameters in the PESs and couplings are fitted to the results of smooth diabatic electronic structure calculations including dynamic electron correlation by the extended multi-configurational quasi-degenerate perturbation theory method for the adiabatic state energies followed by diabatization by the fourfold way. The fit is accomplished by the anchor points reactive potential method with two reactive coordinates and 40 nonreactive degrees of freedom, where the anchor-point force fields are obtained with a locally modified version of the *QuickFF* package. The PESs and couplings are suitable for study of the topography of the trilayer potential energy landscape and for electronically nonadiabatic molecular dynamics simulations of the photodissociation of the S-CH₃ bond. *Published by AIP Publishing.* [<http://dx.doi.org/10.1063/1.4975121>]

I. INTRODUCTION

Nonadiabatic transitions happen most efficiently near conical intersection seams,¹⁻⁵ and the characteristics of coupled potential energy surfaces near such seams are critical for understanding many spectroscopic observables and electronically nonadiabatic processes.⁶⁻²⁷ The photodissociation of thioanisole, as well as that of similar molecules such as phenol, thiophenol, and anisole,²⁸⁻³⁶ is a prototype of the photo-induced hydrogen/methyl detachment and proton transfer reactions mediated by conical intersections between a bound $^1\pi\pi^*$ state and a repulsive $^1\pi\sigma^*$ or $^1n\sigma^*$ state.³⁷⁻⁴⁰ For thioanisole, the role that conical intersections play in the mechanism has been studied both theoretically and experimentally.^{36,41,42} The proposed mechanism can be understood based on Figure 1, a schematic of the relevant adiabatic potential energy surfaces along the S-CH₃ bond stretch coordinate, R . At the equilibrium geometry (with $R \cong 1.8 \text{ \AA}$), the molecule is first excited (by an ultraviolet photon with energy 4.3–4.5 eV) from the closed-shell ground state S_0 to the bound singlet excited state S_1 with $\pi\pi^*$ character. The reactive flux then transfers in the region near the S_1 - S_2 conical intersection (labeled CI1) to the repulsive $n\sigma^*$ state and proceeds to the region near the S_0 - S_1 conical intersection (labeled CI2) with elongated S-CH₃ bond. Finally, the flux bifurcates near CI2, and the molecule dissociates to either the D_0 or D_1 state of thiophenoxyl radical plus methyl radical. In Figure 1 and also in the remainder of this paper, “ $\pi\pi$,” “ $\pi\pi^*$,” and “ $n\sigma^*$ ” are used as diabatic labels based on the character of the diabatic states; the

diabatic potential energy surfaces (PESs) are the diagonal elements of the diabatic potential energy matrix and are denoted by U_{11} , U_{22} , U_{33} . On the other hand, “ S_0 ,” “ S_1 ,” and “ S_2 ” are used as adiabatic labels for the potential energy functions of the adiabatic states, whose PESs are denoted by $V_1 < V_2 < V_3$.

Previous theoretical studies have focused on either the local topography of the PESs at the minimum-energy conical intersection (MECI) geometries or on the global topography of the PESs along only two dimensions, namely the S-CH₃ bond stretch and the C-C-S-C torsion.^{36,41} Although these two coordinates are considered to be the most important “reaction coordinates,” the PESs can still have important dependence on the other 40 “spectator” degrees of freedom. In particular, the conical intersection seam is multi-dimensional in nature, and the reactive flux can access the seam or a low barrier near the seam at geometries where the 40 “spectator” degrees of freedom are away from their values for the equilibrium geometry or the MECI geometry. Therefore, all degrees of freedom can be important for nonadiabatic dynamical simulations. This is a challenge because a set of full-dimensional analytic potential surfaces and couplings has never previously been presented for a system with this many degrees of freedom. We shall address the challenge by using a diabatic representation. The advantage of a diabatic representation is that PESs and state couplings are smooth scalars in a diabatic representation, whereas in an adiabatic representation the PESs have cuspidal ridges at high-dimensional seams of conical intersection, and the state couplings or vectors become singular at these ridges. Note that we define a diabatic representation as one that reduces the coupling of electronic states due to nuclear momentum and nuclear kinetic energy “to a level

^{a)}Email: truhlar@umn.edu

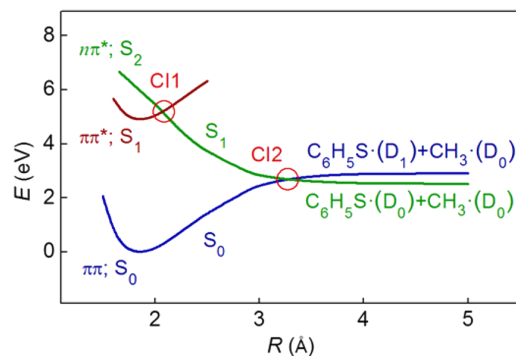


FIG. 1. Schematic cut of the adiabatic potential energy surfaces of thioanisole along the S–C bond stretch coordinate, R .

comparable to the nonadiabatic coupling that occurs in the BO representation in regions where the Born-Oppenheimer approximation is a good approximation⁴³ so they may be neglected, and all the coupling that needs to be retained for a realistic treatment of dynamics comes from the electronic Hamiltonian. Furthermore, we assume that the fourfold way diabaticization scheme⁴⁴ produces a good approximation to such a diabatic representation.

In the present work we present an analytic fit to the full-dimensional diabatic PESs and diabatic state couplings of the three lowest singlet states of thioanisole. Note that, following the usual conventions, the couplings in the diabatic representation are called diabatic couplings, whereas the couplings in the adiabatic representation are called nonadiabatic couplings. The diabatic PESs are diagonal elements of the diabatic potential energy matrix, and the diabatic couplings are off-diagonal elements of this matrix; thus—as mentioned in the previous paragraph—the diabatic PESs and diabatic couplings are scalars. The scalar adiabatic PESs and vector nonadiabatic couplings are also available from these fits since they are easily calculated⁴⁵ by a diabatic-to-adiabatic diagonalization with a small number of states, in particular three states in the present case.

The present fits cover a wide range of geometries from the Franck-Condon region to the dissociation of the S–CH₃ bond. By using the anchor points reactive potential (APRP) scheme developed by our group,^{33,46} we treat two coordinates, which are called reactive coordinates, globally, and we treat other coordinates by system-specific, reaction-coordinate-specific molecular mechanics (MM). In constructing the PESs of thioanisole, we have made two improvements of the APRP scheme as compared to its previous employment: (1) we generalized the scheme, which originally was implemented with one reactive coordinate, to include two reactive coordinates (and the same kind of generalization could be used in the future to treat more than two reactive coordinates); (2) we made the fitting of the potential functions along the non-reactive coordinates much more convenient by using a locally modified version⁴⁷ of the *QuickFF* package⁴⁸ for “automatic” force field generation.

The PESs are full-dimensional in the sense that they are functions of all the 42 internal degrees of freedom of thioanisole. By construction, however, the PESs are most accurate near the anchor points, which are the most impor-

tant for the photodissociation of the S–CH₃ bond. The PESs are not appropriate for study of other reaction channels of thioanisole.

The rest of this paper is arranged as follows. Section II gives the technical details of the construction of the APRP potential energy matrix. Section III compares the APRP potential energy matrix elements and the derived properties, such as equilibrium and saddle point geometries, conical intersections, excitation energies, and vibrational frequencies, with experiment and with electronic structure calculations. Section IV is a summary.

II. METHODS AND COMPUTATIONAL DETAILS

A. Introduction

The APRP can be applied to a single potential energy surface or to a diabatic potential energy matrix, whose diagonal elements are called diabatic potential energy surfaces, and whose off-diagonal elements are called diabatic couplings. The whole potential energy matrix is referred to as the “potential” in this work. In the present case, we fit three diabatic surfaces and their couplings. The APRP scheme involves two steps. In the first step of the present work we fit the diabatic potential energy matrix in the reactive degrees of freedom, which are called the primary and secondary degrees of freedom.

First we review the fitting of a single one of the diabatic potential energy surfaces. The reactive coordinates must be able to describe any bond breaking, bond making, or bond rearrangements and any other coordinates that have wider-amplitude motion than can accurately be described by non-reactive molecular mechanics. The reactive coordinates can be subdivided into two groups: those with a strong coupling to nonreactive degrees of freedom are called primary coordinates, and those, if any, with a negligible coupling to nonreactive degrees of freedom are called secondary coordinates. The method that can be used for fitting the dependence of the surface on the reactive degrees of freedom is completely general and depends on the system under study; for the present application it is described in Section II C 1. The dependence of the potential on the reactive degrees of freedom is fitted with the remaining coordinates fixed, for example, at their equilibrium values in the reactant or product or at partially optimized values with fixed secondary and tertiary coordinates; these remaining coordinates are called the tertiary coordinates.

In the second step we add the dependence of the potential on the tertiary coordinates. This is done by identifying a number of points, called anchor points, specified by their values of the primary and secondary coordinates (the primary coordinates differ among the anchor points, but the secondary coordinates, if any, do not), and fitting a nonreactive molecular mechanics potential to each surface and coupling in the tertiary coordinates at each anchor point. The regional potentials at the anchor points are then sown together into a single tertiary potential by functions called tent functions. In this way the potential as a function of the tertiary coordinates also depends on, i.e., is coupled to, the primary coordinates. To make the procedure more robust, the nonreactive molecular mechanics potential is expressed in terms of Simon-Parr-Finlan

coordinates⁴⁹ for stretches (rather than the usual bare bond extension coordinates) and trigonometric functions³³ for bends (rather than the usual bare bond angles). Because these coordinates extend the region over which the fits are valid, as compared to using the usual internal coordinates, we label the anchor-point fits as regional potentials rather than local potentials. Further details of the tertiary potential fits for the present application are given in Section II C 2.

In the present case, we use one primary coordinate, one secondary coordinate, and a set of 73 or 67 redundant internal coordinates as tertiary coordinates for diabatic potential energy surfaces. We use two primary coordinates, no secondary coordinates, and a set of 8 tertiary coordinates for diabatic couplings. (Details are given in Sections II C 3 and II C 5.) The diabatic potential energy surfaces in the primary coordinates and all the diabatic couplings are fitted to the corresponding quantities obtained by the extended multi-configurational quasi-degenerate perturbation theory (XMC-QDPT)^{50–52} followed by the fourfold way^{44,53–55} and model space diabaticization.⁵⁶ (Details are given in Section II E.) The diabatic potential energy surfaces in the tertiary coordinates are fitted to those computed by Kohn-Sham density functional theory (DFT)^{57,58} and linear-response time-dependent DFT (TDDFT).⁵⁹ (Details are given in Section II E.)

Figure 2(a) shows our convention for numbering the atoms. We do not distinguish elements for the numbering; for instance, we have “C1” and “H9” rather than “C1” and “H1.” We will refer to the atoms by “element + number” (e.g., S7), by number only (e.g., 7), or by element only (e.g., S), depending on the context.

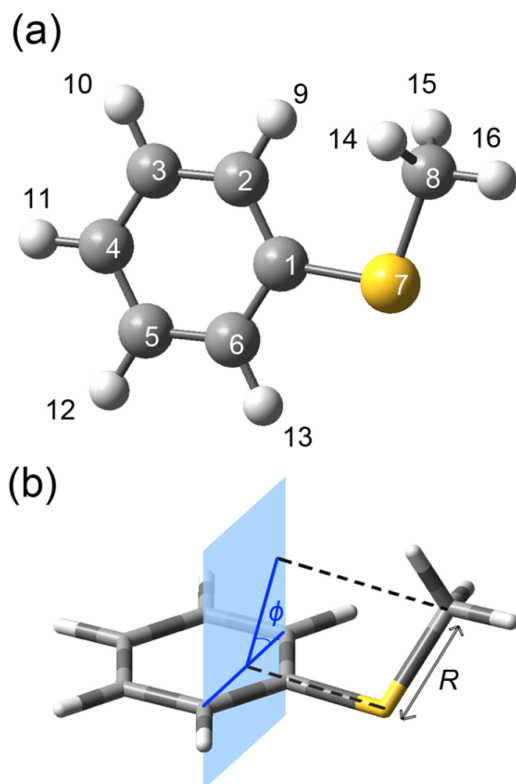


FIG. 2. (a) Numbering of atoms. (b) Definition of coordinates R and ϕ ; the blue plane contains C2 and C6 and is normal to the C6–C1–C2 plane.

B. Primary and secondary coordinates

In the APRP scheme we need to define a set of “reactive” internal coordinates that must be treated globally to describe the reaction; in the present application of the APRP scheme, these are primary and secondary coordinates. Primary coordinates can have arbitrarily large amplitude of motion in the reaction, and they have strong potential energy coupling to other coordinates. Secondary coordinates can have arbitrarily large amplitude of motion in the reaction and are treated globally as well, but they have weaker coupling to coordinates other than the primary ones. For photodissociation of thioanisole, the S–CH₃ bond stretch and C–C–S–C torsion are the conventional internal coordinates that play the most prominent roles. In our previous work⁶⁰ we studied the diabatic PESs of thioanisole along these two coordinates, and we showed that they both play significant roles in the adiabatic-to-diabatic transformation. A more detailed examination, though, shows that the diabatization depends most strongly on the orientation of the S–CH₃ bond relative to the phenyl plane. The C–C–S–C torsion is a good representation of this orientation only when C2, C1, C6, and S are coplanar. Therefore, in the present work, in which these four atoms are not constrained to be coplanar, we use an alternative angular coordinate as a primary or secondary coordinate (secondary for fitting the diabatic potential energy surfaces and primary for fitting the diabatic couplings); in particular, we use the angle between the vector C6–C2 and the projection of vector S–C8 on the plane defined by the vector C6–C2 and the normal vector of the C6–C1–C2 plane. Hereafter we label this angular coordinate as ϕ and the S–C8 bond length as R . They are defined explicitly as

$$R = |\mathbf{r}_{7-8}|, \quad (1)$$

$$\cos \phi = \frac{\mathbf{r}_{6-2} \cdot \mathbf{v}_p}{|\mathbf{r}_{6-2}| |\mathbf{v}_p|},$$

$$\mathbf{v}_p = \mathbf{r}_{7-8} - \mathbf{v}_x \frac{\mathbf{v}_x \cdot \mathbf{r}_{7-8}}{|\mathbf{v}_x|^2}, \quad (2)$$

$$\mathbf{v}_x = \mathbf{r}_{6-2} \times (\mathbf{r}_{6-1} \times \mathbf{r}_{1-2}),$$

where \mathbf{r}_{i-j} is the vector from atom i to atom j . These two coordinates are illustrated in Figure 2(b). For treating the diabatic potential energy surfaces, R is a primary and ϕ is a secondary coordinate, whereas for treating the diabatic couplings, both R and ϕ are primary. The key distinction between the treatments of diabatic potential energy surfaces and diabatic couplings is that the tertiary couplings depend on both R and ϕ , while the tertiary potential energy surfaces depend only on R , as will be discussed in detail in Sections II C 2 and II C 5.

We note that some coordinates involving the S–CH₃ bond such as the C–S–C bond angle can have large amplitude of motion when the S–CH₃ bond stretches and may be treated as secondary coordinates. However, based on the excessive energy of S₁ compared to the dissociation asymptote and our previous work on a similar system, phenol,³² we expect that the molecule will dissociate quickly once it goes past CI1 into the repulsive region and will not have time to distribute energy to such coordinates as the C–S–C bond angle to have large amplitude of motion. Therefore, we treat those coordinates as tertiary coordinates for simplicity. Our

sample trajectories show that the molecule dissociates in less than 0.5 ps after entering the repulsive region, which supports our decision.

C. Anchor points reactive potential (APRP) for constructing the diabatic potential energy matrix

To apply the APRP scheme to thioanisole, the diabatic potential energy matrix elements for diabatic states i and j are written as

$$U_{ij}(R, \phi, \mathbf{Q}) = U_{ij}^{[1,2]}(R, \phi) + U_{ij}^{[3]}(\mathbf{Q}|R, \phi), \quad (3)$$

where R and ϕ denote the two reactive coordinates; \mathbf{Q} denotes collectively all the other internal coordinates, which are the tertiary coordinates; and the notation $f(\mathbf{Q}|R, \phi)$ means a function f of \mathbf{Q} that depends parametrically on R and ϕ .

The diagonal elements of \mathbf{U} are the diabatic potential energy surfaces and the off-diagonal elements are the diabatic couplings. The two terms on the right-hand side of Eq. (3) are respectively called reactive-coordinates diabatic potential energy surfaces and tertiary diabatic potential energy surfaces for $i = j$ and are respectively called primary and tertiary diabatic couplings for $i \neq j$. The reactive-coordinates diabatic potential energy surfaces and primary diabatic couplings are fitted globally with general functional forms. The tertiary diabatic potential energy surfaces and diabatic couplings are fitted regionally with MM functional forms. Standard MM fits are local, by which we mean that they are valid only in a quadratic or near-quadratic region around their central point, except for torsions, which are usually fitted with more widely valid trigonometric functions; our tertiary potential goes beyond standard MM in two ways: (i) we use more widely valid internal coordinates than those usually used in MM; (ii) we tie several such MM fits (each centered at an anchor point) together via tent functions of the primary coordinates. Thus the molecular mechanics expressions in the tertiary diabatic potential energy surfaces depend parametrically on the primary coordinates.

1. Reactive-coordinates diabatic potential energy surfaces and primary diabatic couplings

As mentioned in Section II A, the reactive-coordinates matrix elements are fitted to values calculated by XMC-QDPT followed by fourfold way and model space diabatization. These are single-point calculations at geometries on a two-dimensional grid of R and ϕ values, while the other coordinates are fixed at values of the S_0 equilibrium geometry. These diabatic potential energy surfaces and diabatic couplings are then fitted with general analytic functions.

For diabatic state $\pi\pi$ (corresponding to S_0 in the Franck-Condon region), the surface is fitted with the following function including a Rydberg model potential⁶¹ term:

$$U_{11}^{[1,2]}(R, \phi) = A_1 - D_1[1 + b_1(R - R_{11})]e^{-b_1(R - R_{11})} + B_1 \exp[-\alpha_1(R - R_{12})^2](1 - \cos 2\phi), \quad (4)$$

where $A_1, D_1, b_1, R_{11}, B_1, \alpha_1$, and R_{12} are parameters.

Diabatic state $\pi\pi^*$ (corresponding to S_1 in the Franck-Condon region) is energetically accessible only for small- R

geometries, and it is fitted with the following function including a Morse potential⁶² term:

$$U_{22}^{[1,2]}(R, \phi) = A_2 + D_2(1 - e^{-b_2(R - R_{21})})^2 + B_2 e^{-\alpha_2(R - R_{22})^2}(1 - \cos 2\phi), \quad (5)$$

where $A_2, D_2, b_2, R_{21}, B_2, \alpha_2$, and R_{22} are parameters.

For diabatic state $n\sigma^*$ (corresponding to S_2 in the Franck-Condon region), the surface is fitted with the following function:

$$U_{33}^{[1,2]}(R, \phi) = A_3 + D_3 e^{-b_3 R} + [B_3 e^{-\alpha_3(R - R_3)^2} + C_3 e^{-4\alpha_3(R - R_3)^2}](1 - \cos 2\phi), \quad (6)$$

where $A_3, D_3, b_3, B_3, C_3, \alpha_3$, and R_3 are parameters.

The primary diabatic couplings are fitted with

$$U_{12}^{[1]}(R, \phi) = B_0^{(12)} + B_2^{(12)} \exp[-\alpha_2^{(12)}(R - R_2^{(12)})^2] \sin^2 \phi + B_4^{(12)} \exp[-\alpha_4^{(12)}(R - R_4^{(12)})^2] \sin^4 \phi, \quad (7)$$

$$U_{13}^{[1]}(R, \phi) = B_2^{(13)} \exp[-\alpha_2^{(13)}(R - R_2^{(13)})^2] \sin 2\phi + (c_0^{(13)} + c_1^{(13)} R) \exp[-\alpha_4^{(13)} R] \sin 4\phi, \quad (8)$$

$$U_{23}^{[1]}(R, \phi) = B_4^{(23)} \exp[-\alpha_4^{(23)}(R - R_4^{(23)})^2] \sin 4\phi + B_6^{(23)} \exp[-\alpha_6^{(23)}(R - R_6^{(23)})^2] \sin 6\phi, \quad (9)$$

where $B_k^{(ij)}$, $\alpha_k^{(ij)}$, $R_k^{(ij)}$, and $c_k^{(ij)}$ ($i, j = 1, 2, 3$; k is an integer) are parameters. These functional forms are chosen to have the correct symmetry about $\phi = n\pi/2$ (where n is an integer, including zero), namely U_{12} is even and U_{13} and U_{23} are odd. (See the [supplementary material](#) for the explanation of this symmetry.)

2. Tertiary diabatic potential energy surfaces

The tertiary diabatic potential energy surfaces are constructed via interpolation of MM-like potentials modeled at predetermined anchor point geometries, each of which has primary and secondary coordinates fixed at certain values (referred to as ‘‘anchor point nodes’’ for the individual primary and secondary coordinates and as ‘‘anchor point locations’’ for the set of primary and secondary coordinates) and tertiary coordinates relaxed by partial geometry optimization.

The tertiary diabatic potential energy surfaces are given by

$$U_{ii}^{[3]}(\mathbf{Q}|R) = \sum_{a=1}^{A(ii)} U_{ii}^{[3](a)}(\mathbf{Q}) T^{(a)}\left(R, \{R_a^{(ii)}\}_{a=1}^{A(ii)}\right), \quad (10)$$

where $A(ii)$ is the number of anchor point nodes for fitting $U_{ii}^{[3]}$, where $\{R_a^{(ii)}\}_{a=1}^{A(ii)}$ is the set of the nodes specifying these anchor points, $U_{ii}^{[3](a)}$ is tertiary surface i at anchor point node a , and T , called a tent function, gives the weight of the anchor point node in the interpolation. The tent functions are given by

$$T^{(1)}\left(q, \{q_a\}_{a=1}^A\right) = \begin{cases} 1, & q < q_1 \\ \frac{(q - q_2)^4}{(q - q_2)^4 + (q - q_1)^4}, & q_1 \leq q < q_2 \\ 0, & \text{otherwise} \end{cases} \quad (11)$$

$$T^{(a)}(q, \{q_a\}_{a=1}^A) = \begin{cases} \frac{(q - q_{a-1})^4}{(q - q_a)^4 + (q - q_{a-1})^4}, & q_{a-1} \leq q < q_a \\ \frac{(q - q_{a+1})^4}{(q - q_{a+1})^4 + (q - q_a)^4}, & q_a \leq q < q_{a+1} \\ 0, & \text{otherwise} \end{cases} \quad \text{for } a = 2, \dots, A-1, \quad (12)$$

$$T^{(A)}(q, \{q_a\}_{a=1}^A) = \begin{cases} \frac{(q - q_{A-1})^4}{(q - q_A)^4 + (q - q_{A-1})^4}, & q_{A-1} \leq q < q_A \\ 1, & q > q_A \\ 0, & \text{otherwise} \end{cases} \quad (13)$$

where q_a is the value of q at anchor point node a , and the anchor point nodes are arranged in ascending order of q_a .

The tertiary surface $U_{ii}^{[3](a)}$ at an anchor point location is modeled by force field terms whose parameters are optimized to reproduce the Hessian matrix at a partially optimized anchor point geometry calculated by DFT and TDDFT. (The procedure of optimizing the parameters will be discussed later in this section.) In particular, it is written as

$$U_{ii}^{[3](a)} = U_{\text{rel},ii}^{[3](a)} + U_{ii}^{S(a)} + U_{ii}^{B(a)} + U_{ii}^{T(a)} + U_{ii}^{D(a)}, \quad (14)$$

where $U_{\text{rel},ii}^{[3](a)}$ is the energy of the partially optimized anchor point geometry relative to the geometry with primary and secondary coordinates fixed at their anchor point values and tertiary coordinates fixed at values corresponding to the S_0 equilibrium geometry. Notice that Eq. (14) does not contain the optional van der Waals terms or electrostatic terms of the *QuickFF* procedure; they could be included in the general case but were deemed unnecessary for the present problem. The last four terms on the right-hand side of Eq. (14) are contributions from bond stretches, valence angle bends, torsions, and out-of-plane distances (defined as the distance d from one atom to the plane formed by another three atoms).⁴⁸ These terms are given respectively by

$$U_{ii}^{S(a)}(\{R_\mu\}) = \frac{1}{2} \sum_{\mu} k_{\mu,ii}^{S(a)} \left(\frac{R_\mu - R_{0,\mu ii}^{(a)}}{R_\mu} \right)^2, \quad (15)$$

$$U_{ii}^{B(a)}(\{\theta_\mu\}) = \frac{1}{2} \sum_{\mu} k_{\mu,ii}^{B(a)} (\cos \theta_\mu - \cos \theta_{0,\mu ii}^{(a)})^2, \quad (16)$$

$$U_{ii}^{T(a)}(\{\phi_\mu\}) = \frac{1}{2} \sum_{\mu} k_{\mu,ii}^{T(a)} (1 - \cos [n_\mu(\phi_\mu - \phi_{0,\mu ii}^{(a)})]), \quad (17)$$

$$U_{ii}^{D(a)}(\{d_\mu\}) = \frac{1}{2} \sum_{\mu} k_{\mu,ii}^{D(a)} (d_\mu - d_{0,\mu ii}^{(a)})^2, \quad (18)$$

where μ runs over the appropriate tertiary coordinates (note that Eq. (17) is equivalent to Eq. (14c) of Ref. 33); the k quantities are force constants, the variables with a subscript 0 are force field parameters representing the position of the minimum of the term, and the n parameters are dihedral multiplicities. The dihedral multiplicities are predetermined based on local or regional symmetry, and the force constants and minimum-position parameters are determined by the fitting

procedure described in Section II C 3 rather than fixed at values for the partially optimized anchor point geometry. The functional forms of the stretches, valence bends, and torsions terms in Eqs. (15)–(18) have better global behavior than simple harmonic terms. Notice that the force field used here has no cross terms that couple different tertiary coordinates; this would be a poor approximation if made in Cartesian coordinates, but it is much safer to neglect cross terms when one uses internal coordinates.⁶³

The tertiary coordinates used are all the (redundant) bond stretches, valence bends, torsions, and out-of-plane distances based on the connectivity of the atoms shown in Figure 2. They are listed in Table I along with the dihedral multiplicities.

3. Determination of force field parameters for tertiary diabatic potential energy surfaces

A four-step procedure is used to determine the force field parameters for the tertiary diabatic potential energy surface of each diabatic state. (1) A set of anchor point values of R is chosen. (2) An anchor point geometry is obtained for each anchor point value of R by partial geometry optimization on the corresponding adiabatic state using DFT or TDDFT with the constraint that R is fixed at the chosen node and ϕ fixed at 0° . (In the original *QuickFF* procedure, force fields are constructed around one location, which is the equilibrium geometry. Here with multiple anchor point locations, partial optimization is needed for each anchor point.) (3) The Cartesian Hessian matrix is obtained for each partially optimized anchor point geometry by DFT or TDDFT. (4) The force field parameters are optimized against the DFT or TDDFT Hessian matrix. This procedure is repeated for each of the three diabatic states.

For step (1), anchor point nodes of $R = 1.8, 2.2, 3.2,$ and 6.0 \AA are chosen for $U_{11}^{[3]}$, $R = 1.8$ and 2.2 \AA for $U_{22}^{[3]}$, and $R = 1.9, 2.2, 3.2,$ and 6.0 \AA for $U_{33}^{[3]}$. All these anchor point geometries have C_s symmetry, for which we can model the dependence of the diagonal diabatic potentials on the tertiary coordinates as being the same as the dependence of the adiabatic potentials on these coordinates; therefore we use the Hessian matrix of the adiabatic state for modeling the tertiary diabatic potential energy surfaces. The first anchor point value is chosen to be at or near the S_0 equilibrium value of 1.8 \AA . (1.9 \AA is chosen for $U_{33}^{[3]}$ because at $R = 1.8 \text{ \AA}$ the partial geometry optimization for this state does not converge.) The last anchor point is chosen in the asymptotic region, and the geometry optimizations at this anchor point were carried out separately for the thiophenoxyl and methyl radicals.

Step (4) was carried out by using our own modified version⁴⁷ of the *QuickFF* package.⁴⁸ For each anchor point, *QuickFF* takes as input the anchor point geometry, the set of internal coordinates and the corresponding force field

TABLE I. Tertiary coordinates used for modeling tertiary diabatic potential energy surfaces.^a

Coordinate type	Tertiary coordinates for anchor points with $R \neq 6.0 \text{ \AA}$ ^b	Tertiary coordinates for anchor points with $R = 6.0 \text{ \AA}$ ^c
Bond stretches	C–C (6), C–H (8), C1–S7	C–C (6), C–H (8), C1–S7
Valence bends	C–C–C (6), C–C–H (10), C–C–S (2), C–S–C, S–C–H (3), H–C–H (3)	C–C–C (6), C–C–H (10), C–C–S (2), H–C–H (3)
Torsions ^d	C–C–C–C (6,2), C–C–C–H (10,2), C–C–C–S (2,2), H–C–C–H (4,2), H–C–C–S (2,2), C–S–C–H (3,3)	C–C–C–C (6,2), C–C–C–H (10,2), C–C–C–S (2,2), H–C–C–H (4,2), H–C–C–S (2,2)
Out-of-plane distance ^e	H9–C1–C3–C2, H10–C2–C4–C3, H11–C3–C5–C4, H12–C4–C6–C5, H13–C1–C5–C6, S7–C2–C6–C1	H9–C1–C3–C2, H10–C2–C4–C3, H11–C3–C5–C4, H12–C4–C6–C5, H13–C1–C5–C6, S7–C2–C6–C1, H14–H15–H16–C8

^aFor bond stretches and valence bends, the number in parentheses, if given, is the number of coordinates of the given type; for example, C–C (6) means six C–C bond stretches are used. If no number is given there is just one.

^bInternal coordinates are chosen based on the connectivity in Figure 2.

^cInternal coordinates are chosen based on the connectivity in Figure 2 except that C7 and C8 are disconnected due to R being large.

^dThe first number in parentheses is the number of coordinates of the given type, and the second number in parentheses is the dihedral multiplicity.

^eNotation for out-of-plane distances: $a-b-c-d$ denotes the distance from atom d to the $a-b-c$ plane.

functions in Eqs. (15)–(18), and the *ab initio* Cartesian Hessian matrix. The internal coordinates are the tertiary coordinates listed in Table I, plus the S7–C8 bond stretch, the C2–C1–S7–C8 torsion, and the C6–C1–S7–C8 torsion for anchor points with $R \neq 6.0 \text{ \AA}$. The last three coordinates are closely correlated with primary and secondary coordinates. They are needed for *QuickFF* to construct the force field, but their corresponding potential functions are replaced by the reactive-coordinates surface terms when the reactive-coordinates and tertiary diabatic potential energy surfaces are combined for the full surface. *QuickFF* optimizes the force field parameters by optimizing the Cartesian Hessian derived from the force field against the *ab initio* Hessian. The details of how *QuickFF* derives force field parameters using information in the *ab initio* Hessian matrix can be found in Ref. 48. With our improved force field functional forms, the procedure is essentially the same, except that the simple quadratic functions in Eqs. (2.11) and (2.12) of Ref. 44 are replaced by our improved functions, with the parameters to be fitted being the ones in Eqs. (15)–(18) of this paper. For asymptotic anchor points with $R = 6.0 \text{ \AA}$, we use force constants derived from isolated thiophenoxyl and methyl radicals in order that the diabatic potential energy surfaces will have the correct asymptotic behavior.

4. Born-Mayer potential

To avoid the non-bonded carbons from coming too close during a trajectory, we added additional Born-Mayer potentials between all pairs of *para* carbon atoms (C1–C4, C2–C5, C3–C6) to all diagonal elements of the diabatic potential energy matrix. The Born-Mayer potential is given by

$$V_{\text{BM}} = B \sum_{i-j=1-4,2-5,3-6} \exp(-\alpha r_{i-j}), \quad (19)$$

where the parameters are set to $B = 42\,000 \text{ kcal mol}^{-1}$ and $\alpha = 3.58 \text{ \AA}^{-1}$.⁶⁴

5. Tertiary diabatic couplings

Similar to tertiary diabatic potential energy surfaces, tertiary diabatic couplings are built by interpolating the couplings modeled at preselected anchor point locations. However, the set of anchor point locations for the tertiary couplings is different from the set used for tertiary diabatic potential energy surfaces, and throughout Section II C 5 we will use the term “anchor point locations” to refer to this set for tertiary couplings rather than to the set for tertiary surfaces. Unlike those for tertiary diabatic potential energy surfaces, the anchor point geometries for couplings differ from the S_0 equilibrium geometry only in the values of R and ϕ ; the tertiary coordinates are not optimized for fitting the couplings. The expression for the tertiary couplings is

$$U_{ij}^{[3]}(\mathbf{Q}|R, \phi) = s_{ij}(\phi) \sum_{a=1}^2 \sum_{b=1}^3 U_{ij}^{[3](a,b)}(\mathbf{Q}) \left(T^{(a)} \left(R, \{R_a^C\}_{a=1}^2 \right) \right) \times \left(T^{(b)} \left(y(\phi), \{y_b^C\}_{b=1}^3 \right) \right), \quad i \neq j, \quad (20)$$

$$y(\phi) = -\cos 2\phi,$$

$$y_b^C = -\cos 2\phi_b^C.$$

The argument of the second tent function is chosen to be $y = -\cos 2\phi$ so that it has the correct periodicity along ϕ and so that the argument is monotonically increasing in $\phi \in [0, \pi/2]$. Equation (20) can describe the tertiary diabatic couplings for geometries of any ϕ value by choosing anchor point nodes of ϕ only in $[0, \pi/2]$. The additional multiplicative factor s_{ij} is given by

$$s_{12}(\phi) = 1, \quad (21)$$

$$s_{13}(\phi) = s_{23}(\phi) = \text{sign}(\sin 2\phi),$$

where the sign function is defined by

$$\text{sign}(x) = \begin{cases} 1, & x > 0 \\ 0, & x = 0 \\ -1, & x < 0 \end{cases}. \quad (22)$$

The s_{ij} factor is introduced because U_{12} is even and U_{13} and U_{23} are odd about $\phi = n\pi/2$ (where n is an integer, including

zero). The double sum over anchor points in Eq. (21) will be constructed, as described in Section II C 6, such that it is zero at $\phi = n\pi/2$ (where n is an integer, including zero) and that the s_{ij} factor does not cause discontinuity.

The $U_{ij}^{[3]}$ so defined have periodicity along ϕ because of the definition of y in Eq. (20) and the s_{ij} factor in Eq. (21). Such periodicity exists only for a relaxed scan along ϕ , where the molecule has C_s symmetry for $\phi = 0^\circ$ or 90° . In practice, however, we make an approximation of assuming such periodicity for general geometries in the anchor point interpolation along ϕ .

A set of nonredundant internal coordinates is used to expand the tertiary diabatic couplings. These coordinates are different from those used for the tertiary diabatic potential energy surfaces. We examined the magnitude of diabatic couplings introduced by changing each angular coordinate (valence bends, torsions, and out-of-plane bends), and we chose only eight coordinates that are symmetric and make the most significant contributions to the variations of the couplings; these are listed in Table II.

The diabatic coupling at an anchor point, $U_{ij}^{[3](a,b)}$, is a sum of terms, each term corresponding to one coordinate,

$$U_{ij}^{[3](a,b)}(\mathbf{Q}) = \sum_{\mu} U_{ij,\mu}^{[3](a,b)}(Q_{\mu}). \quad (23)$$

For most coordinates Q_{μ} , the corresponding term in the sum is a second-degree polynomial damped by a Gaussian function,

$$U_{ij,\mu}^{[3](a,b)}(Q_{\mu}) = \left[K_{1,\mu ij}^{(a,b)} (Q_{\mu} - Q_{e,\mu}) + K_{2,\mu ij}^{(a,b)} (Q_{\mu} - Q_{e,\mu})^2 \right] \times \exp \left[- (Q_{\mu} - Q_{e,\mu})^2 / \sigma^2 \right], \quad (24)$$

where the K parameters are to be fitted and the parameters with subscript e are fixed at values for the S_0 equilibrium geometry. The Gaussian function is used to damp the diabatic couplings when $(Q_{\mu} - Q_{e,\mu})$ is large, because the polynomial may have too large values for those unphysical distorted geometries. The

parameter σ is set to 100° so that it does not compromise the physical region with small $(Q_{\mu} - Q_{e,\mu})$.

For the C–S–C bending coordinate (coordinate 8 in Table II), however, the term is a second-degree polynomial of the cosine of the coordinate,

$$U_{ij,\mu}^{[3](a,b)}(Q_{\mu}) = \left[K_{1,\mu ij}^{(a,b)} (\cos Q_{\mu} - \cos Q_{e,\mu}) + K_{2,\mu ij}^{(a,b)} (\cos Q_{\mu} - \cos Q_{e,\mu})^2 \right], \quad (25)$$

for $Q_{\mu} = \theta_{\text{CSC}}$.

The reason for this treatment is that $\cos \theta_{\text{CSC}}$ has better behavior for large amplitude motion of θ_{CSC} , which can occur as R increases and the S–CH₃ bond weakens.

6. Determination of force field parameters for tertiary diabatic couplings

A three-step procedure, different from the modified *QuickFF* procedure used for the tertiary diabatic potential energy surfaces, is used to numerically fit the polynomial coefficients in Eqs. (24) and (25). (1) A set of anchor point locations is chosen and the corresponding anchor point geometries are built. Every pair of (R_a^C, ϕ_b^C) corresponds to an anchor point location. Every anchor point geometry has primary coordinates specified by the anchor point location, with the other coordinates fixed at values of S_0 equilibrium geometry. (Partial optimization is not used in this fit.) (2) For each anchor point geometry, each coordinate in Table II is in turn displaced by $-30^\circ, -20^\circ, -10^\circ, -5^\circ, -4^\circ, -3^\circ, -2^\circ, -1^\circ, 1^\circ, 2^\circ, 3^\circ, 4^\circ, 5^\circ, 10^\circ, 20^\circ, 30^\circ$ and the tertiary diabatic couplings are computed by XMC-QDPT followed by the fourfold way and model space diabatization. (3) The K parameters in Eqs. (24) and (25) are determined by fitting Eq. (24) or (25) to the difference of the *ab initio* data from step (2) and the primary diabatic couplings.

For step (1), we choose $R_a^C = 1.97$ and 3.5 \AA and $\phi_b^C = 0^\circ, 10^\circ, 45^\circ, 80^\circ, \text{ and } 90^\circ$ as anchor point nodes. The two anchor point nodes of R are chosen to be near the two conical intersections where the state couplings are most important.

TABLE II. Coordinates along which tertiary diabatic couplings are modeled.^a

Coordinate	Coordinate type	Description	Symmetry ($\phi = 0^\circ$) ^b	Symmetry ($\phi = 90^\circ$) ^c
1	Out-of-plane bend	$\theta_{7-1-6-2}$ ^d	a''	a'
2	Ring puckering	$\varphi_{1-2-3-4} - \varphi_{2-3-4-5} + \varphi_{3-4-5-6}$ $-\varphi_{4-5-6-1} + \varphi_{5-6-1-2} - \varphi_{6-1-2-3}$	a''	a''
3	Ring asymmetric torsion	$-\varphi_{1-2-3-4} - \varphi_{2-3-4-5} + 2\varphi_{3-4-5-6}$ $-\varphi_{4-5-6-1} - \varphi_{5-6-1-2} + 2\varphi_{6-1-2-3}$	a''	NS
4	Ring asymmetric bend	$-\theta_{1-2-3} + 2\theta_{2-3-4} - \theta_{3-4-5}$ $-\theta_{4-5-6} + 2\theta_{5-6-1} - \theta_{6-1-2}$	a'	NS
5	Ring asymmetric bend	$-\theta_{1-2-3} + \theta_{3-4-5}$ $-\theta_{4-5-6} + \theta_{6-1-2}$	a'	NS
6	Asymmetric bend	$\theta_{2-1-12} - \theta_{6-1-12}$	a'	a''
7	Ring asymmetric torsion	$-\varphi_{1-2-3-4} + \varphi_{2-3-4-5}$ $-\varphi_{4-5-6-1} + \varphi_{5-6-1-2}$	a''	NS
8	Bend	θ_{1-7-8}	a'	a'

^aIn the table, φ denotes torsion, θ denotes bond angle, NS stands for "not symmetric," and symmetries are for the C_s point group.

^b C_s point group for geometries where $\phi = 0^\circ$ and the symmetry plane is the coplanar C₆H₅SC.

^c C_s point group for geometries where $\phi = 90^\circ$ and the C–S–C symmetry plane is perpendicular to the coplanar C₆H₅S.

^dOut-of-plane angle between vector C1–S7 and plane C1–C6–C2. The sign is determined by the sign of $(\mathbf{v}_{6-1} \times \mathbf{v}_{1-2}) \cdot \mathbf{v}_{1-7}$, where \mathbf{v}_{i-j} is the vector pointing from atom i to atom j .

TABLE III. Vertical excitation energies (in eV) of thioanisole.^a

Method	S ₀ -S ₁ (2 A')	S ₀ -S ₂ (1 A'')	Reference
APRP ^b	4.56	5.02	This work
EOM-CCSD/aug-cc-pV(T+d)Z	4.84	5.21	69
TD-M06-2X/MG3S	4.94	5.05	69
TD-B3LYP/maTZ	4.60	4.82	69
TDA-τ-HCTHhyb/6-31+G*	4.65	4.97	69
SA(3)-MC-QDPT(12,11)/maTZ	4.64	5.13	69
SA(3)-XMC-QDPT(12,11)/maTZ	4.64	5.13	69
SA(3)-MC-QDPT(12,11)/aug-cc-pV(T+d)Z	4.52	5.02	69
CR-EOM-CCSD(T)/aug-cc-pV(T+d)Z	4.53	5.03	69

^aAll data are calculated at the equilibrium geometry optimized by M06-2X/MG3S, unless specified otherwise. The references for methods and basis sets not described in this paper can be found in Ref. 69.

^bCalculated at the equilibrium geometry optimized by APRP.

For steps (2) and (3), for each anchor point location with $\phi_b^C = 10^\circ, 45^\circ, \text{ or } 80^\circ$, *ab initio* calculations were carried out and the K parameters in Eqs. (24) and (25) are determined by fitting Eq. (24) or (25) to the difference of the *ab initio* diabatic couplings and the already-determined primary diabatic couplings. For each anchor point location with $\phi_b^C = 0^\circ$ or 90° , the K parameters are set to zero so that $U_{ij,\mu}^{[3](a,b)} = 0$ and that the s_{ij} factor in Eq. (20) does not cause discontinuity.

D. Gradients, adiabatic potentials, and nonadiabatic couplings

The gradients of diabatic matrix elements with respect to Cartesian coordinates are given by the chain rule

$$\frac{\partial U_{ij}}{\partial x_\alpha} = \sum_\mu \frac{\partial U_{ij}}{\partial q_\mu} \frac{\partial q_\mu}{\partial x_\alpha}, \quad (26)$$

where x_α and q_μ are Cartesian and internal coordinates and μ runs over all internal coordinates on which U_{ij} depends. The derivatives $\partial q_\mu / \partial x_\alpha$ are given by the Wilson B matrix,⁶⁵ which is coded in the FORTRAN PES subroutine.

The adiabatic potentials are obtained by diagonalizing the diabatic potential energy matrix,

$$V_i = \sum_j \sum_k C_{ji} U_{jk} C_{ki}, \quad (27)$$

where \mathbf{C} is the orthogonal matrix that diagonalizes \mathbf{U} .

The gradients of adiabatic potentials and the nonadiabatic couplings are given by⁴⁵

$$\frac{\partial V_i}{\partial x_\alpha} = \sum_j \sum_k C_{ji} \frac{\partial U_{jk}}{\partial x_\alpha} C_{ki}, \quad (28)$$

TABLE IV. S₀-S₁ adiabatic and 0-0 excitation energies (in eV) of thioanisole.^a

	Adiabatic	0-0
APRP	4.35	4.08
SA(3)-XMC-QDPT/maTZ//CASSCF/maTZ	4.36	4.22
Expt. ^b	...	4.28

^aSee text for definition of adiabatic and 0-0 excitation energies.

^bReference 36.

TABLE V. Geometric parameters of the S₀ equilibrium geometry of thioanisole.

	APRP	M06-2X ^a	Electron diffraction ^b	Electron diffraction ^c
Bond lengths (Å)				
C1-C2	1.407	1.392	1.402 ^d	1.391
C2-C3	1.405	1.390	1.399 ^d	1.391
C3-C4	1.400	1.385	1.395 ^d	1.391
C4-C5	1.405	1.391	1.399 ^d	1.391
C5-C6	1.398	1.383	1.393 ^d	1.391
C6-C1	1.412	1.397	1.406 ^d	1.391
C1-S7	1.765	1.761	1.775	1.749
S7-C8	1.827	1.797	1.813	1.803
C-H (average)	1.092	1.084	1.120	1.096
Bond angles (deg)				
C1-C2-C3	119.9	120.0	120.2	120.0
C2-C3-C4	120.7	120.8	120.8	120.0
C3-C4-C5	119.3	119.2	119.3	120.0
C4-C5-C6	120.5	120.4	120.6	120.0
C5-C6-C1	120.3	120.4	119.8	120.0
C6-C1-C2	119.3	119.1	119.3	120.0
C1-S7-C8	102.9	102.9	104.5	105.6

^aBasis set: MG3S.

^bReference 89.

^cReference 85.

^dThis experiment did not distinguish the different C-C bonds in the phenyl; these values were refined using B3LYP.

$$F_{ij}^\alpha = \langle \psi_i | \frac{\partial}{\partial x_\alpha} | \psi_j \rangle = \begin{cases} \frac{1}{V_j - V_i} \sum_k \sum_l C_{ki} \frac{\partial U_{kl}}{\partial x_\alpha} C_{lj} & (i \neq j) \\ 0 & (i = j) \end{cases}, \quad (29)$$

where $|\psi_i\rangle$ is the i th adiabatic state. A proof of Eq. (28) is given in the [supplementary material](#).

TABLE VI. Geometric parameters of the S₁ equilibrium geometry of thioanisole.

	APRP	TD-τ-HCTHhyb ^a
Bond lengths (Å)		
C1-C2	1.408	1.400
C2-C3	1.455	1.446
C3-C4	1.426	1.418
C4-C5	1.407	1.400
C5-C6	1.457	1.448
C6-C1	1.432	1.421
C1-S7	1.758	1.758
S7-C8	1.809	1.800
C-H (average)	1.094	1.094
Bond angles (deg)		
C1-C2-C3	117.7	117.4
C2-C3-C4	118.6	118.4
C3-C4-C5	122.9	123.3
C4-C5-C6	119.4	119.3
C5-C6-C1	116.8	116.4
C6-C1-C2	124.6	125.2
C1-S7-C8	107.0	107.0

^aBasis set: jul-cc-pV(D+d)Z. Imaginary frequency of 53i cm⁻¹ is present for the C-C-S-C torsional mode.

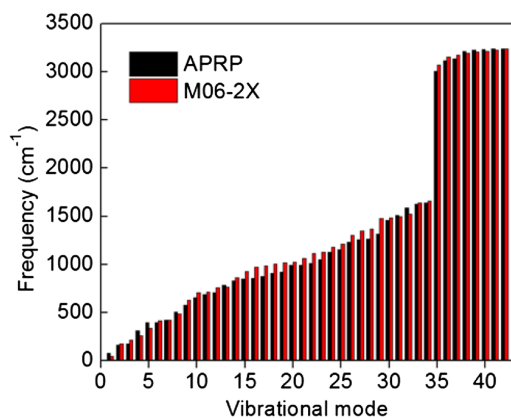


FIG. 3. Frequencies of S_0 equilibrium geometry of thioanisole computed by APRP and by DFT with M06-2X.

E. Additional computational details

The *ab initio* data used for constructing the reactive-coordinates diabatic potential energy surfaces and all the diabatic couplings were calculated by extended multiconfigurational quasidegenerate perturbation theory (XMC-QDPT) followed by the fourfold way and model space diabaticization, with a mixed, minimally augmented basis set of 6-311+G(d)^{66,67} for carbon and hydrogen and MG3S⁶⁸ for sulfur, denoted by maTZ in this paper (standing for minimally augmented triple zeta). (The same basis set was denoted by MB in Refs. 60 and 69.) Details of the calculations such as active orbitals and diabatic prototypes, as well as detailed discussion about the diabaticization, can be found in Refs. 56 and 60. The GAMESS^{70,71} electronic structure package was used for these calculations.

The partial geometry optimizations and Hessian calculations for constructing the tertiary diabatic potential energy surfaces were performed by Kohn-Sham DFT for the ground state and linear-response TDDFT for the excited states. The M06-2X^{72,73} exchange-correlation functional and the jul-cc-pV(D+d)Z⁷⁴⁻⁷⁷ basis set were used for DFT. The τ -HCTHhyb⁷⁸ functional and the jul-cc-pV(D+d)Z basis set were used for TDDFT. The Gaussian 09⁷⁹ electronic structure package was used for these calculations.

The minimum energy conical intersections (MECIs) between adiabatic states i and j are obtained by minimizing

TABLE VII. Energies and geometric parameters of the S_1 saddle point and S_1 - S_2 MECI.

Coordinate	S_1 saddle point	S_1 - S_2 MECI
V_2^a (eV)	4.33	4.53
R^b (Å)	1.909	1.959
ϕ^c (deg)	23.1	0.0
$\varphi_{2-1-7-8}^d$ (deg)	32.9	0.0
$\varphi_{1-2-3-4}$ (deg)	7.9	0.0
$\theta_{7-1-6-2}^e$ (deg)	11.0	0.0

^aAdiabatic potential energy of S_1 relative to the S_0 energy at the S_0 equilibrium geometry.

^bS7-C8 bond length.

^cSee Section II B for definition.

^dTorsions.

^eCoordinate 1 in Table II.

TABLE VIII. Values of primary and secondary coordinates at some key geometries.

Geometry	Description ^a	R (Å)	ϕ (deg)
1	Planar minimum	1.809	0.0
2	Saddle point 1	1.811	6.1
3	Nonplanar minimum	1.867	22.0
4	Saddle point 2	1.909	23.1
5	Point along MEP ^b at 0.529 Å from geometry 4	2.023	24.1
6	Point along MEP ^b at 1.038 Å from geometry 4	2.087	25.4

^aMinimum geometries, saddle point geometries, and MEP optimized with the APRP PES.

^bMinimum energy path scaled to a reduced mass of 1 amu.

the following function using an in-house BFGS optimizer:⁸⁰

$$\frac{V_i + V_j}{2} + \alpha(V_i - V_j)^2, \quad (30)$$

where V_i is the adiabatic energy of state i and the parameter α is set to $10^5 E_h^{-2}$.

The geometry optimization, vibrational analysis, and minimum energy path calculations with the fitted APRP potential matrices were done with POLYRATE.⁸¹ We have run thousands of sample trajectories with the APRP potential matrices interfaced to ANT⁸² to ensure they conserve energy and do not visit unphysical geometries.

III. RESULTS AND DISCUSSION

A. Excitation energies in the Franck-Condon region

Tables III and IV compare the vertical, adiabatic, and 0–0 excitation energies given by APRP to various electronic structure methods and to experiment. Here vertical excitation energy is defined as the difference of potential energies at the S_0 equilibrium geometry; adiabatic energy is defined as the difference of potential energies of S_1 and S_0 at their respective equilibrium geometry (S_2 is not considered since it does not have a minimum); 0–0 excitation energy is defined as the adiabatic excitation energy plus the difference of zero-point vibrational energy of S_1 and S_0 at their respective equilibrium geometry. (The zero point energies are computed in the harmonic approximation.)

Table III shows that APRP compares well with the best estimates of vertical excitation energy, which are the ones given by completely renormalized equation-of-motion coupled cluster theory with singles, doubles, and non-iterative connected triples (CR-EOM-CCSD(T))^{83,84} with the aug-cc-pV(T+d)Z basis set⁷⁴⁻⁷⁷ and by SA(3)-MC-QDPT(12,11)/aug-cc-pV(T+d)Z. Table IV shows that the adiabatic excitation energy given by APRP also compares well with XMC-QDPT, while the 0–0 excitation energy is underestimated by 0.2 eV compared to experiment. This deviation is presumably due to the difficulty of modeling the topography and thus the vibrational frequencies of S_1 , as will be discussed in Section III B.

B. Equilibrium geometries and vibrational frequencies

Whether the equilibrium geometry of S_0 has the methyl carbon in the phenyl plane (with C_s symmetry) or out of the

TABLE IX. V_2 (eV) at some important geometries as given by APRP and by electronic structure methods.^a

Geometry ^b	APRP	XMC-QDPT/maTZ	TD- τ -HCTHhyb /jul-cc-pV(D+d)Z
1	4.1370	4.1227	3.9972
2	4.1376	4.1239	3.9974
3	4.1142	3.9802	4.0489
4	4.1152	4.0002	4.0931
5	4.0795	4.0739	4.1875
6	4.0380	4.0171	4.0705

^aEnergies are relative to V_1 at geometry 1 given by the respective methods.^bSee Table VIII for description of the geometries.

plane is a question that has been under debate for years. The older literature concluded that it is out of the plane,⁸⁵ but more recent experimental and theoretical studies consistently agree on the opposite.^{86–89} Our geometry optimization by M06-2X/MG3S leads to a C_s geometry, which is consistent with the recent experimental and theoretical studies.

Geometry optimization with our fitted APRP PES of S_0 also leads to a C_s geometry. Table V lists the bond lengths and bond angles of the equilibrium geometry of S_0 given by APRP, by M06-2X, and by experiments. APRP compares quite well with experiment, with errors less than 0.01 Å and 0.5° for most bond lengths and bond angles. Larger deviations from the experiment values from Ref. 89 occur for the S7–C8 (0.014 Å

and C–H (0.028 Å) bond lengths and the C1–S7–C8 (1.6°) bond angle. The deviations of the C–H bond length and the C1–S7–C8 bond angle are due to the deviation of the *ab initio* values to which APRP is fitted. The deviation of the S7–C8 bond length is due to the fact that its *ab initio* value is not used explicitly in the fitting. Nevertheless, all the deviations are small.

The equilibrium geometry of S_1 ($\pi\pi^*$ in the Franck-Condon region) is a more complicated issue. Experimentally the electronic spectrum exhibits resolved $S_1 \leftarrow S_0$ origin band structure⁴¹ and the origin band further shows resolved rotational structure.⁸⁷ The observed rotational constants in S_1 are similar to those in S_0 , which implies that S_1 is a bound state with an equilibrium geometry not too different from the S_0 one. Our CASSCF/maTZ geometry optimization also resulted in an S_1 equilibrium geometry with C_s symmetry similar to that of S_0 . However, geometry optimization by TDDFT with various functionals (M06-2X, τ -HCTHhyb, B3LYP) and basis sets (6-31+G(d), jun-cc-pV(D+d)Z, maTZ) was not successful. Optimizations with a C_s symmetry constraint all resulted in one imaginary frequency for the C–C–S–C out-of-plane torsional mode. Optimizations without symmetry constraint went through a S_1 - S_2 conical intersection and were unable to locate a minimum for the $\pi\pi^*$ state. This disagrees with the experimental findings. The reason is likely to be that the barrier separating the S_1 minimum from the S_1 - S_2 conical intersection is very small and thus hard to calculate accurately. This barrier is likely to be located along the C–C–S–C torsional path,

TABLE X. Adiabatic energies and geometric parameters of S_0 - S_1 conical intersections along a path with selected R values.^a

R (Å)	V_1 (eV)	V_2 (eV)	V_3 (eV)	ϕ (deg)	θ_{2-1-7} (deg)	Ring puckering ^b (deg)	Ring asym. torsion 1 ^c (deg)	Ring asym. torsion 2 ^d (deg)
3.0	3.14	3.14	7.03	0.0	114.1	9.3	-41.4	-21.6
3.1	2.95	2.95	6.91	0.0	111.9	0.5	-3.7	-4.8
3.2	2.89	2.89	6.81	0.0	106.3	0.6	-0.8	-2.0
3.3	2.90	2.90	6.79	0.0	104.6	-0.4	0.2	-1.4
3.4	2.97	2.97	6.83	0.0	103.4	-0.7	-0.8	-3.6
3.5	3.06	3.06	6.90	0.0	102.6	-2.2	-1.6	-3.3

^aSee text for details of the path. Adiabatic energies are relative to V_1 at the S_0 equilibrium geometry.^bCoordinate 2 in Table II.^cCoordinate 3 in Table II.^dCoordinate 7 in Table II.TABLE XI. Adiabatic energies and geometric parameters of S_0 - S_1 conical intersections along a path with selected $\varphi_{2-1-7-8}$ values.^a

$\varphi_{2-1-7-8}$ (deg)	V_1 (eV)	V_2 (eV)	V_3 (eV)	R (Å)	ϕ (deg)	θ_{2-1-7} (deg)	Ring puckering ^b (deg)	Ring asym. torsion 1 ^c (deg)	Ring asym. torsion 2 ^d (deg)
0	2.88	2.88	6.81	3.217	0.0	108.9	0.0	0.0	0.0
5	2.90	2.90	6.79	3.220	0.0	109.3	-12.2	19.3	-6.2
10	2.94	2.94	6.82	3.221	0.0	110.4	-17.7	23.4	-15.1
15	3.03	3.03	6.85	3.294	8.2	104.6	-5.4	8.3	-46.1
20	3.07	3.07	6.88	3.271	8.4	107.0	-11.0	15.0	-49.7

^aSee text for details of the path. Adiabatic energies are relative to V_1 at the S_0 equilibrium geometry.^bCoordinate 2 in Table II.^cCoordinate 3 in Table II.^dCoordinate 7 in Table II.

because our CASSCF/maTZ calculation gives the frequency of the corresponding torsional mode to be as low as 22 cm^{-1} . Failure of TDDFT to calculate this shallow potential well leads to the negative frequency along the torsional mode. Nevertheless, we fitted the tertiary APRP potential to the geometry optimized with the C_s constraint and the Cartesian Hessian matrix computed by TD- τ -HCTHhyb. The resulting tertiary surface does not have the correct terms for the C-C-S-C torsional motion. However, these terms essentially correspond to the secondary coordinate ϕ , and they are therefore replaced by the reactive-coordinates surface terms in the full surface.

Table VI compares the bond lengths and bond angles of the S_1 equilibrium geometry optimized with APRP to those obtained with TDDFT. APRP matches well with TDDFT, to which the tertiary diabatic potential energy surfaces are fitted, with most deviations within 0.01 \AA for bond lengths and 0.5° for bond angles. This accuracy is also achieved for the D_0 and D_1 states of the thiophenoxyl radical shown in Tables S1 and S2 in the [supplementary material](#). These results are very encouraging for the ability of APRP to fit complex-molecule potential energy surfaces.

Figure 3 compares APRP and DFT for the vibrational frequencies of the thioanisole S_0 state. (Similar comparisons were made for S_1 of thioanisole and D_0 and D_1 of the thiophenoxyl radical, and they are given in the [supplementary material](#).) Although the parameters of the tertiary APRP surface are fitted to the M06-2X frequencies, they do not perfectly match because of the restricted form of the tertiary surface (especially the lack of cross terms between internal

coordinates). Nonetheless, the median signed and absolute percentage deviations in the 42 frequencies are -4% and 5% respectively, and 38 of the 42 frequencies are well reproduced with a deviation of less than 10% . APRP gives the frequency of the C-C-S-C torsional mode of the S_1 equilibrium geometry to be 38 cm^{-1} , a small value consistent with the preceding discussion.

C. S_1 saddle point geometry separating equilibrium and repulsive regions

Previous work^{36,41} has indicated the important role of the S_1 - S_2 conical intersection at $R \sim 2\text{ \AA}$ in the dynamics; it was proposed that the photodissociation starts with a reactive flux from the bound $\pi\pi^*$ state to the repulsive $n\pi^*$ state through the conical intersection. However, we emphasize that the reactive flux need not go through the conical intersection. In fact, when moving away from the conical intersection in the branching space, the energy of the lower state often decreases as the degeneracy is lifted, and such a decrease is found in the present case. Thus, there is often a saddle point on the shoulder of a conical intersection,⁹⁰⁻⁹² and such a saddle point is found here. Therefore, the barrier on the S_1 PES separating the equilibrium and repulsive regions is likely to occur at a geometry near, but not at, the conical intersection seam.

The optimization of saddle points on an excited state PES is a very difficult task for electronic structure methods because it requires calculation of the excited state Hessian. With the analytic APRP PESs, however, we are able to do it with little computational cost. The energies and geometric parameters

TABLE XII. Adiabatic energies and geometric parameters of S_1 - S_2 conical intersections along a path with selected R values.^a

R (\AA)	V_1 (eV)	V_2 (eV)	V_3 (eV)	ϕ (deg)	θ_{2-1-7} (deg)	Ring puckering ^b (deg)	Ring asym. torsion 1 ^c (deg)	Ring asym. torsion 2 ^d (deg)
1.8	1.79	5.53	5.53	0.0	98.0	-53.5	-60.0	55.8
1.9	0.48	4.78	4.78	0.0	99.1	-0.6	1.0	-3.5
2.0	0.54	4.62	4.62	0.0	107.0	2.4	-2.2	3.8
2.1	0.87	4.83	4.83	0.0	105.7	0.0	0.0	0.0
2.2	1.58	5.21	5.21	0.0	106.5	5.5	-8.2	1.1

^aSee text for details of the path. Adiabatic energies are relative to V_1 at the S_0 equilibrium geometry.

^bCoordinate 2 in Table II.

^cCoordinate 3 in Table II.

^dCoordinate 7 in Table II.

TABLE XIII. Adiabatic energies and geometric parameters of S_1 - S_2 conical intersections along a path with selected $\varphi_{2-1-7-8}$ values.^a

$\varphi_{2-1-7-8}$ (deg)	V_1 (eV)	V_2 (eV)	V_3 (eV)	R (\AA)	ϕ (deg)	θ_{2-1-7} (deg)	Ring puckering ^b (deg)	Ring asym. torsion 1 ^c (deg)	Ring asym. torsion 2 ^d (deg)
0	0.31	4.53	4.53	1.959	0.0	105.2	0.0	0.0	0.0
5	0.33	4.53	4.53	1.960	0.0	105.8	-9.0	10.4	-0.1
10	0.35	4.55	4.55	1.954	8.7	105.5	-26.7	26.4	14.0
15	0.38	4.57	4.57	1.952	12.4	105.9	-39.4	41.1	5.7
20	0.42	4.60	4.60	1.943	20.3	105.9	-47.3	49.3	19.0

^aSee text for details of the path. Adiabatic energies are relative to V_1 at the S_0 equilibrium geometry.

^bCoordinate 2 in Table II.

^cCoordinate 3 in Table II.

^dCoordinate 7 in Table II.

of the S_1 saddle point and the S_1 - S_2 MECI optimized with the APRP PES are listed in Table VII. The saddle point is 0.20 eV lower than the MECI, with a similar S-CH₃ distance R . Previous work has indicated the possibility that such a saddle point may be located with a large value of the C-C-S-C torsion.⁴¹ This is indeed the case in our calculation. Moreover, the C₆H₅S moiety is significantly distorted from planar. For instance, the C1-C2-C3-C4 torsion is 7.9°, and there is an angle of 11.0° between the C1-S7 bond and the C6-C1-C2 plane.

In terms of energies relative to the S_0 equilibrium geometry, the saddle point is 4.33 eV while the S_1 equilibrium geometry is 4.35 eV. The reason that the saddle point is lower in energy than the equilibrium geometry of S_1 is that there is another saddle point (4.36 eV) and another local minimum (4.33 eV) near the equilibrium, located on a path corresponding to the torsional motion of C-C-S-C. The aforementioned “true” saddle point leading to dissociation is between the 4.33 eV local minimum and the repulsive region. Recalling the preceding discussion of the difficulty of modeling the S_1 PES around its equilibrium geometry, the existence of the 4.36 eV saddle point and the 4.33 eV local minimum is likely due to the minor unsmoothness of the S_1 PES. Nevertheless, a difference of 0.02 eV should not have a significant effect on the dynamics.

To ensure that the profile of the APRP PES of S_1 in the Franck-Condon region is reasonable, we selected a set of plots at which we compare V_2 (which is the adiabatic potential energy of S_1) as computed by APRP with its value computed by several high-level *ab initio* methods. The geometries are specified in Table VIII, and the comparison is in Table IX, which shows that V_2 of APRP, which is fitted to data from XMC-QDPT and TD- τ -HCTHhyb, but not at these geometries, deviates from these two methods by only ~ 0.1 eV or less.

D. Conical intersections

The MECIs are important qualitative features of the PESs. We optimized the S_1 - S_2 MECI (MECI1, belonging to the CI1 seam in Figure 1) and the S_0 - S_1 MECI (MECI2, belonging to the CI2 seam in Figure 1) with the fitted APRP PESs. Both MECIs have C_s symmetry, with R equal to 1.96 Å at MECI1 and 3.22 Å at MECI2.

In addition to the MECIs, with the fitted full-dimensional PESs, we can also map cuts of the conical intersection seams along some paths. As illustrations, here we map one-dimensional cuts of the S_1 - S_2 CI1 seam and the S_0 - S_1 CI2

seam along two paths. The first path is determined by minimizing Eq. (30) with R fixed at certain values and other coordinates relaxed. The second path is determined by minimizing Eq. (30) with the bond lengths r_{2-1} and r_{1-7} and the

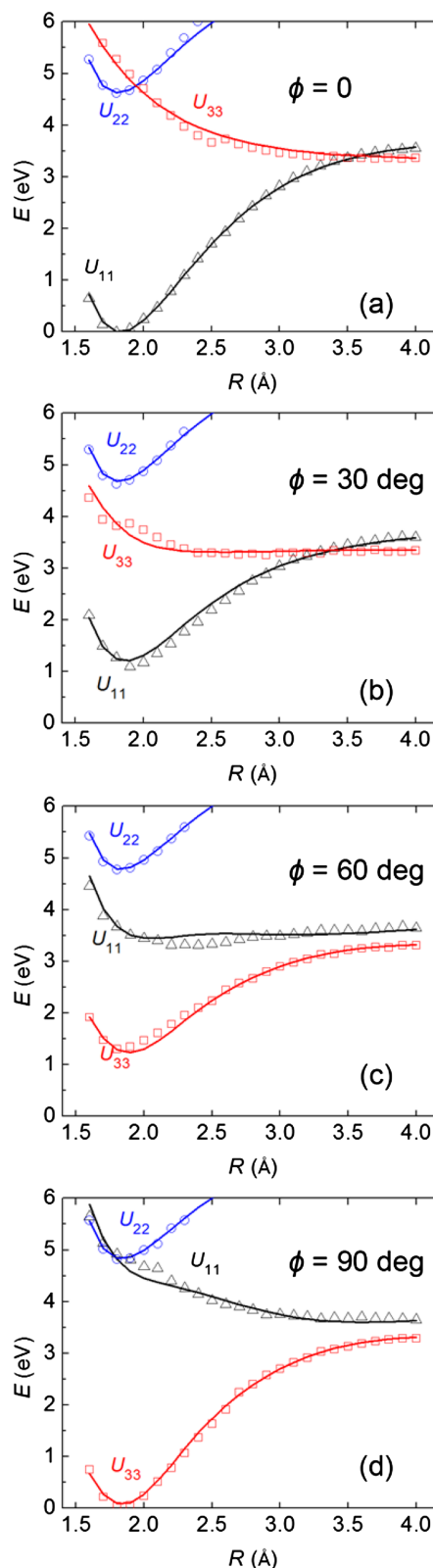


FIG. 4. Diabatic potential energy curves given by APRP (solid lines) and XMC-QDPT/maTZ (open symbols) along R for different values of ϕ . (Other internal coordinates are fixed at values for the S_0 equilibrium geometry.)

TABLE XIV. Adiabatic energies^a given by APRP and XMC-QDPT of the S_0 - S_1 conical intersections along a path with selected R values.^b

R (Å)	APRP		XMC-QDPT/maTZ	
	V_1	V_2	V_1	V_2
3.0	3.14	3.14	3.08	3.43
3.1	2.95	2.95	2.94	3.15
3.2	2.89	2.89	2.88	3.04
3.3	2.90	2.90	2.88	2.99

^aEnergies in eV relative to those for the S_0 equilibrium geometry.

^bGeometries are the same as the first four in Table X.

bond angle θ_{2-1-7} fixed at the equilibrium values for S_0 , with the torsion $\varphi_{2-1-7-8}$ fixed at certain values, and with the other coordinates relaxed. The two paths are computed for each of the two conical intersection seams, which yield four one-dimensional conical intersection cuts.

The adiabatic energies and some geometric parameters along these four cuts are given in Tables X–XIII. The geometric parameters include the coordinates R and ϕ , the C–S–C bend θ_{2-1-7} , and three torsional coordinates of the ring that measure its distortion from planar. It can be clearly seen that away from the MECI of states i and j , the adiabatic energies of the two states increase, and the C_6 ring becomes more distorted.

Table XIV compares the adiabatic energies of S_0 and S_1 given by the APRP model and by XMC-QDPT for the geometries in Table X. The mean unsigned deviation of the APRP energies from the XMC-QDPT ones is 0.10 eV, and the deviation is less than 0.30 eV even for the significantly distorted geometry with $R = 3.0$ Å. Note that the location of conical intersections is sensitive to potential energies, so it is not surprising that conical intersections within the APRP model are not precisely degenerate in XMC-QDPT; the seams are slightly shifted.

E. Cuts of adiabatic and diabatic potential energy surfaces and diabatic couplings

To evaluate the quality of our fitting, Figures 4–6 compare the diabatic potential energy curves, diabatic couplings,

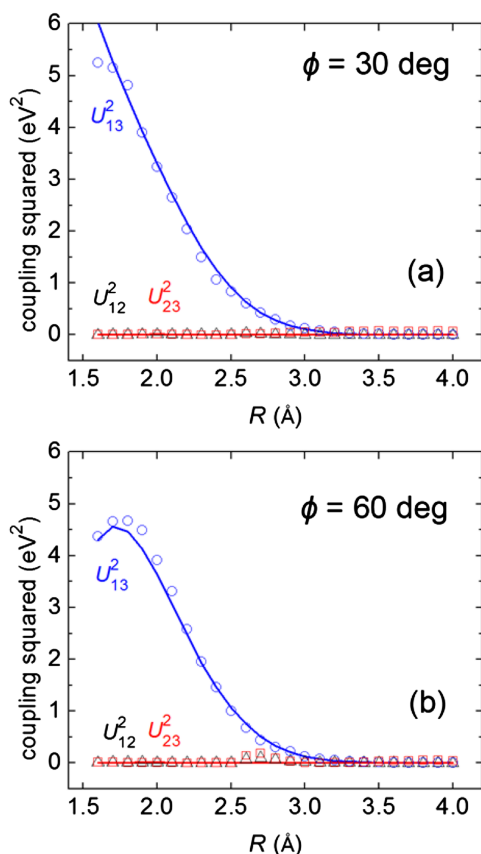


FIG. 5. Diabatic couplings given by APRP (solid lines) and XMC-QDPT/maTZ (open symbols) along R for different values of ϕ . (Other internal coordinates are fixed at values for the S_0 equilibrium geometry. Those for $\phi = 0^\circ$ and 90° are not shown since the couplings are negligible in those cases.)

and adiabatic potential energy curves given by APRP and XMC-QDPT along R with four ϕ values and with the other coordinates fixed at their values for the S_0 equilibrium geometry. The fit is very good for $\phi = 0^\circ$. For $\phi \neq 0$, the error is larger

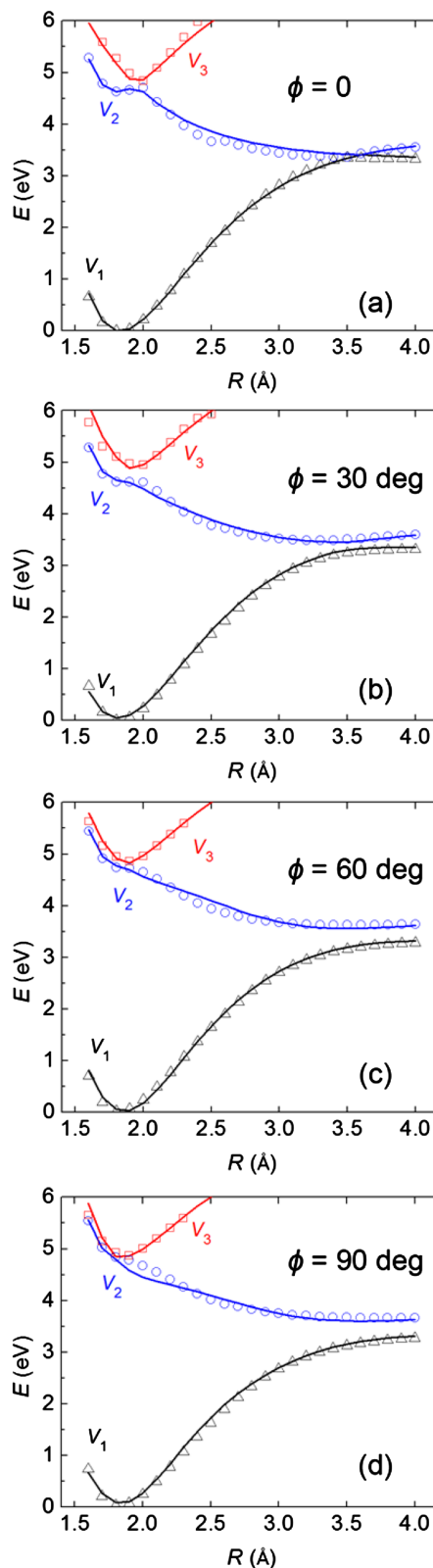


FIG. 6. Adiabatic potential energy curves given by APRP (solid lines) and XMC-QDPT/maTZ (open symbols) along R for different values of ϕ . (Other internal coordinates are fixed at values for the S_0 equilibrium geometry.)

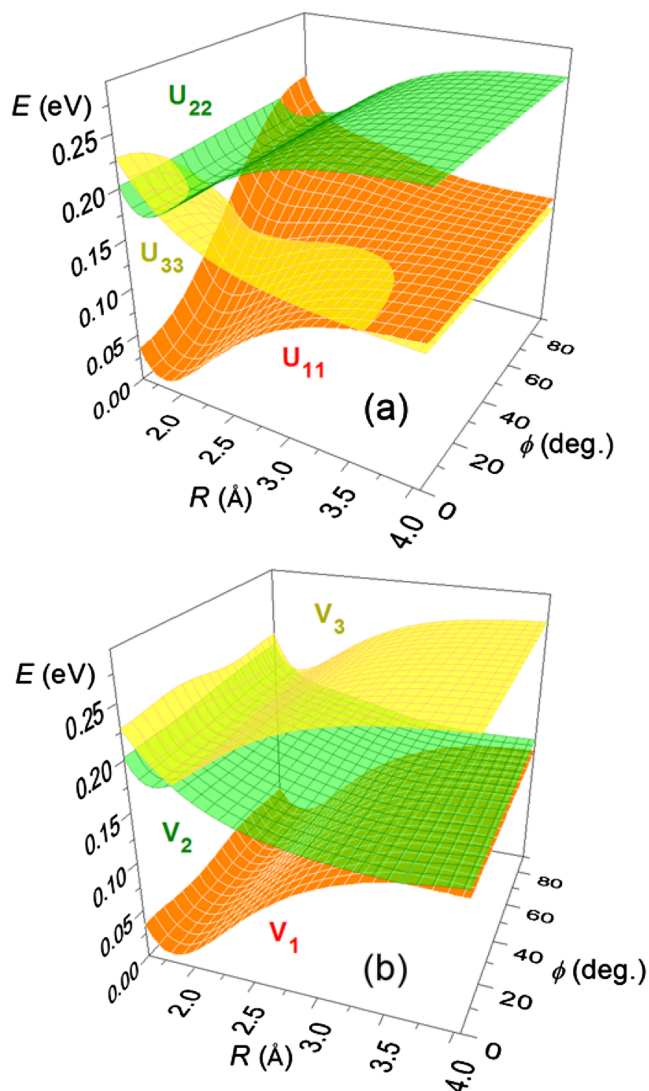


FIG. 7. APRP diabatic (a) and adiabatic (b) PESs along R and ϕ . (Other internal coordinates are fixed at values for the S_0 equilibrium geometry.)

where the XMC-QDPT data are less smooth. The U_{13} for $R < 1.7$ Å and $\phi = 30^\circ$ in Figure 5(a) has noticeable error, but the two diabatic potential energies U_{11} and U_{33} at those points are widely separated so that the error in the diabatic couplings does not affect the adiabatic energies much, as can be seen in Figure 6(b). The small bump in U_{12}^2 and U_{23}^2 between $R = 2.5$ and 3.0 Å in Figure 5(b) is an artifact due to a crossing

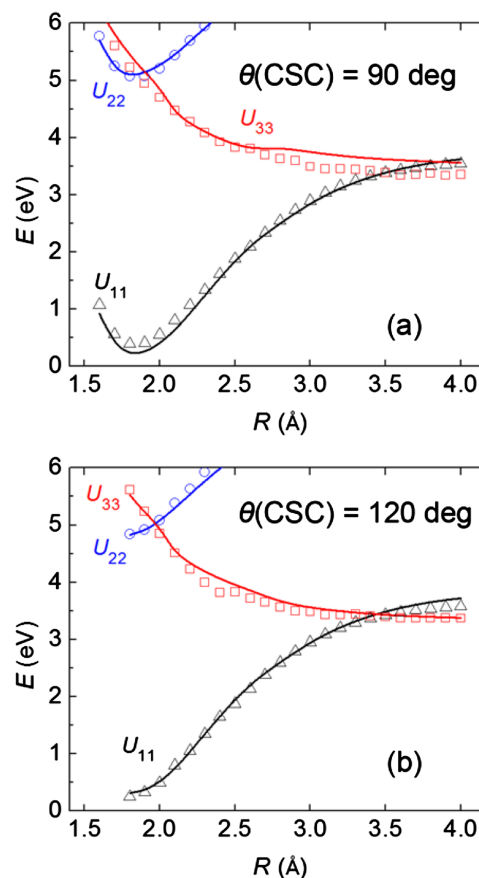


FIG. 8. Diabatic potential energy curves given by APRP (solid lines) and XMC-QDPT/maTZ (open symbols) along R for two values of the C–S–C bond angle not equal to its value for the S_0 equilibrium geometry. (Other internal coordinates are fixed at values for the S_0 equilibrium geometry.)

of the second diabatic state ($\pi\pi^*$) with a higher state that is not computed, and thus the bump is intentionally not fitted. Overall these plots show that the fit is satisfactory. Figure 7 shows the overall topography of the diabatic and adiabatic PESs along R and ϕ .

Next we test our fit outside the set of training data. Figure 8 shows diabatic potential energy curves along R with the C–S–C bond angle (θ_{C-S-C}) not equal to its value for the S_0 equilibrium geometry (103°) and with the other coordinates fixed at their values for the S_0 equilibrium geometry. For $\theta_{C-S-C} = 120^\circ$ the fit remains in good agreement with XMC-QDPT. For $\theta_{C-S-C} = 90^\circ$ the error is larger but still in an acceptable

TABLE XV. Adiabatic energies and geometric parameters of S_1 - S_2 conical intersections along a path with selected R values.^a

R (Å)	ϕ (deg)	θ_{2-1-7} (deg)	Ring puckering ^b (deg)	Coord. 3 ^c (deg)	Coord. 7 ^d (deg)	APRP (eV)			XMC-QDPT/ maTZ (eV)		
						V_1	V_2	V_3	V_1	V_2	V_3
1.831	-1.3	110.0	0.8	-2.3	-1.0	0.62	4.66	5.28	0.37	4.47	5.52
1.781	-2.2	104.9	-0.9	0.8	-3.3	0.41	4.67	5.30	0.18	4.49	5.45

^aAdiabatic energies are relative to V_1 at the S_0 equilibrium geometry.

^bCoordinate 2 in Table II.

^cCoordinate 3 in Table II (ring asymmetric torsion).

^dCoordinate 7 in Table II (ring asymmetric torsion).

range (~ 0.2 eV). As an additional test, we compared adiabatic energies by APRP and XMC-QDPT for two distorted geometries arbitrarily selected from a trajectory. The geometric parameters and the energies are listed in Table XV. The mean unsigned difference between APRP and XMC-QDPT is 0.21 eV for these geometries not in the training set, which is consistent with the accuracy of the APRP fit observed in the other tests.

IV. SUMMARY

In this work, we constructed analytic full-dimensional diabatic potential energy surfaces and state couplings of the three lowest singlet electronic states of thioanisole by using an improved APRP scheme. The diabatic potential energy surfaces and diabatic couplings form a 3×3 matrix of scalar functions of the internal coordinates and were fitted for geometries extending from the Franck-Condon region to the asymptote for breaking the S-CH₃ bond; they are thus suitable for the study of the dissociation of the bond following photo-excitation. Various tests confirm that the APRP PESs are usefully accurate compared to *ab initio* calculations and experimental data. The analytic representations allowed us to optimize upper surface saddle points and trace out the potential energy surfaces along seams of conical intersection. The PESs can be interfaced with software packages such as ANT for dynamical simulations in either the diabatic or adiabatic representation.^{32,82}

SUPPLEMENTARY MATERIAL

See [supplementary material](#) for the determination of symmetries of diabatic couplings along ϕ and comparison of vibrational frequencies of S₁ of thioanisole and D₀ and D₁ of the thiophenoxyl radical given by APRP and density functional methods. A Fortran routine for the potential and its gradients is also provided. The Fortran subroutine is also available from the online POTLIB library at <https://comp.chem.umn.edu/potlib/>.

ACKNOWLEDGMENTS

The authors are grateful to Xuefei Xu, Ke R. Yang, Jingjing Zheng, Chad Hoyer, Junwei Lucas Bao, and Rubén Meana Pañeda for many helpful discussions. This work was supported in part by the U.S. Department of Energy, Office of Basic Energy Sciences, under Grant No. DE-SC0008666. S.L.L. was also supported by the Frieda Martha Kunze Fellowship and a Doctoral Dissertation Fellowship at the University of Minnesota. Computational resources were provided by the University of Minnesota Supercomputing Institute and by the DOE Office of Science User Facilities at Molecular Science Computing Facility in the William R. Wiley Environmental Molecular Sciences Laboratory of Pacific Northwest National Laboratory and at the National Energy Research Scientific Computing Center (Contract No. DE-AC02-05CH11231).

¹E. Teller, *J. Phys. Chem.* **41**, 109 (1937).

²*Conical Intersections: Theory, Computation, and Experiment*, edited by W. Domcke, D. R. Yarkony, and H. Köppel (World Scientific, Hackensack, NJ, 2011).

³S. Matsika and P. Krause, *Annu. Rev. Phys. Chem.* **62**, 621 (2011).

⁴W. Domcke and D. R. Yarkony, *Annu. Rev. Phys. Chem.* **63**, 325 (2012).

⁵L. Blancafort, *ChemPhysChem* **15**, 3166 (2014).

⁶C. E. Caplan and M. S. Child, *Mol. Phys.* **23**, 249 (1972).

⁷C. Sannen, G. Raşeev, C. Galloy, G. Fauville, and J.-C. Lorquet, *J. Chem. Phys.* **74**, 2402 (1981).

⁸H. Köppel, L. S. Cederbaum, and W. Domcke, *J. Chem. Phys.* **77**, 2014 (1982).

⁹V. Bonačić-Koutecký and J. Michl, *Theor. Chim. Acta* **68**, 45 (1985).

¹⁰N. C. Blais, D. G. Truhlar, and C. A. Mead, *J. Chem. Phys.* **89**, 6204 (1988).

¹¹S. Yabushita and K. Morokuma, *Chem. Phys. Lett.* **153**, 517 (1988).

¹²G. Hirsch, R. J. Buenker, and C. Petrongolo, *Mol. Phys.* **73**, 1085 (1991).

¹³M. Braunstein, P. J. Hay, R. L. Martin, and R. T. Pack, *J. Chem. Phys.* **95**, 8239 (1991).

¹⁴M. R. Manaa and D. R. Yarkony, *J. Chem. Phys.* **97**, 715 (1992).

¹⁵D. W. Schwenke, S. L. Mielke, G. J. Tawa, R. S. Friedman, P. Halvick, and D. G. Truhlar, *Chem. Phys. Lett.* **203**, 565–572 (1993).

¹⁶S. L. Mielke, G. J. Tawa, D. G. Truhlar, and D. W. Schwenke, *J. Am. Chem. Soc.* **115**, 6436 (1993).

¹⁷S. L. Mielke, G. J. Tawa, D. G. Truhlar, and D. W. Schwenke, *Int. J. Quantum Chem., Symp.* **27**, 621 (1993).

¹⁸W. Domcke, A. L. Sobolewski, and C. Woywod, *Chem. Phys. Lett.* **203**, 220 (1993).

¹⁹M. Olivucci, I. N. Ragazos, F. Bernardi, and M. A. Robb, *J. Am. Chem. Soc.* **115**, 3710 (1993).

²⁰H. Köppel, *Faraday Discuss.* **127**, 35 (2004).

²¹A. Toniolo, S. Olsen, I. Manohar, and T. J. Martinez, *Faraday Discuss.* **127**, 149 (2004).

²²A. Migani, A. Sinocropi, N. Ferré, A. Cembran, M. Garavelli, and M. Olivucci, *Faraday Discuss.* **127**, 179 (2004).

²³D. G. Truhlar, *Faraday Discuss.* **127**, 227 (2004).

²⁴J. Wei, J. Riedel, A. Kuczmann, F. Renth, and F. Temps, *Faraday Discuss.* **127**, 267 (2004).

²⁵D. R. Yarkony, *Faraday Discuss.* **127**, 325 (2004).

²⁶I. Burghardt, L. S. Cederbaum, and J. T. Hynes, *Faraday Discuss.* **127**, 395 (2004).

²⁷V. Kokoouline and C. H. Greene, *Faraday Discuss.* **127**, 413 (2004).

²⁸Z. Lan, W. Domcke, V. Vallet, A. L. Sobolewski, and S. Mahapatra, *J. Chem. Phys.* **122**, 224315 (2005).

²⁹M. G. D. Nix, A. L. Devine, B. Cronin, R. N. Dixon, and M. N. R. Ashfold, *J. Chem. Phys.* **125**, 133318 (2006).

³⁰O. P. J. Vieuxmaire, Z. Lan, A. L. Sobolewski, and W. Domcke, *J. Chem. Phys.* **129**, 224307 (2008).

³¹X. Xu, K. R. Yang, and D. G. Truhlar, *J. Chem. Theory Comput.* **9**, 3612 (2013).

³²X. Xu, J. Zheng, K. R. Yang, and D. G. Truhlar, *J. Am. Chem. Soc.* **136**, 16378 (2014).

³³K. R. Yang, X. Xu, J. Zheng, and D. G. Truhlar, *Chem. Sci.* **5**, 4661 (2014).

³⁴I. S. Lim, J. S. Lim, Y. S. Lee, and S. K. Kim, *J. Chem. Phys.* **126**, 034306 (2007).

³⁵R. Omidyan and H. Rezaei, *Phys. Chem. Chem. Phys.* **16**, 11679 (2014).

³⁶J. S. Lim and S. K. Kim, *Nat. Chem.* **2**, 627 (2010).

³⁷A. L. Sobolewski and W. Domcke, *Chem. Phys. Lett.* **315**, 293 (1999).

³⁸A. L. Sobolewski and W. Domcke, *Chem. Phys.* **259**, 181 (2000).

³⁹A. L. Sobolewski and W. Domcke, *J. Phys. Chem. A* **105**, 9275 (2001).

⁴⁰A. L. Sobolewski, W. Domcke, C. Dedonder-Lardeux, and C. Jouvet, *Phys. Chem. Chem. Phys.* **4**, 1093 (2002).

⁴¹G. M. Roberts, D. J. Hadden, L. T. Bergendahl, A. M. Wenge, S. J. Harris, T. N. V. Karsili, M. N. R. Ashfold, M. J. Paterson, and V. G. Stavros, *Chem. Sci.* **4**, 993 (2013).

⁴²A. M. Wenge, T. N. V. Karsili, J. D. Rodriguez, M. I. Cotterell, B. Marchetti, R. N. Dixon, and M. N. R. Ashfold, *Phys. Chem. Chem. Phys.* **17**, 16246 (2015).

⁴³B. K. Kendrick, C. A. Mead, and D. G. Truhlar, *Chem. Phys.* **277**, 31 (2002).

⁴⁴H. Nakamura and D. G. Truhlar, *J. Chem. Phys.* **115**, 10353 (2001).

⁴⁵A. W. Jasper and D. G. Truhlar, in *Conical Intersections: Theory, Computation, and Experiment*, edited by W. Domcke, D. R. Yarkony, and H. Köppel (World Scientific, Singapore, 2011), p. 375.

⁴⁶K. R. Yang, X. Xu, and D. G. Truhlar, *J. Chem. Theory Comput.* **10**, 924 (2014).

⁴⁷S. L. Li and D. G. Truhlar, *QuickFFmn 2016* (<http://comp.chem.umn.edu/abcrate/>) based on *QuickFF* – version 1.0.1 (<http://molmod.github.io/QuickFF/>) as described in Ref. 45.

⁴⁸L. Vanduyfhuys, S. Vandenbrande, T. Verstraelen, R. Schmid, M. Waroquier, and V. Van Speybroeck, *J. Comput. Chem.* **36**, 1015 (2015).

⁴⁹G. Simons, R. G. Parr, and J. M. Finlan, *J. Chem. Phys.* **59**, 3229 (1973).

- ⁵⁰H. Nakano, *J. Chem. Phys.* **99**, 7983 (1993).
- ⁵¹H. Nakano, *Chem. Phys. Lett.* **207**, 372 (1993).
- ⁵²A. A. Granovsky, *J. Chem. Phys.* **134**, 214113 (2011).
- ⁵³H. Nakamura and D. G. Truhlar, *J. Chem. Phys.* **117**, 5576 (2002).
- ⁵⁴H. Nakamura and D. G. Truhlar, *J. Chem. Phys.* **118**, 6816 (2003).
- ⁵⁵K. R. Yang, X. Xu, and D. G. Truhlar, *Chem. Phys. Lett.* **573**, 84 (2013).
- ⁵⁶S. L. Li, D. G. Truhlar, M. W. Schmidt, and M. S. Gordon, *J. Chem. Phys.* **142**, 064106 (2015).
- ⁵⁷P. Hohenberg and W. Kohn, *Phys. Rev. B* **136**, B864 (1964).
- ⁵⁸W. Kohn and L. J. Sham, *Phys. Rev.* **140**, A1133 (1965).
- ⁵⁹M. E. Casida, in *Recent Advances in Density Functional Methods, Part I*, edited by D. P. Chong (World Scientific, Singapore, 1995), p. 155.
- ⁶⁰S. L. Li, X. Xu, C. E. Hoyer, and D. G. Truhlar, *J. Phys. Chem. Lett.* **6**, 3352 (2015).
- ⁶¹Y. P. Varshni, *Rev. Mod. Phys.* **29**, 664 (1957).
- ⁶²P. M. Morse, *Phys. Rev.* **34**, 57 (1929).
- ⁶³D. G. Truhlar, R. W. Olson, A. C. Jeannotte II, and J. Overend, *J. Am. Chem. Soc.* **98**, 2373–2379 (1976).
- ⁶⁴S. Gupta, K. Dharamvir, and V. K. Jindal, *Int. J. Mod. Phys. B* **18**, 1021 (2004).
- ⁶⁵E. B. Wilson, J. Decius, and P. Cross, *Molecular Vibrations* (McGraw-Hill, New York, 1955).
- ⁶⁶R. Krishnan, J. S. Binkley, R. Seeger, and J. A. Pople, *J. Chem. Phys.* **72**, 650 (1980).
- ⁶⁷T. Clark, J. Chandrasekhar, G. W. Spitznagel, and P. V. R. Schleyer, *J. Comput. Chem.* **4**, 294 (1983).
- ⁶⁸B. J. Lynch, Y. Zhao, and D. G. Truhlar, *J. Phys. Chem. A* **107**, 1384 (2003).
- ⁶⁹S. L. Li, X. Xu, and D. G. Truhlar, *Phys. Chem. Chem. Phys.* **17**, 20093 (2015).
- ⁷⁰M. W. Schmidt, K. K. Baldrige, J. A. Boatz, S. T. Elbert, M. S. Gordon, J. H. Jensen, S. Koseki, N. Matsunaga, K. A. Nguyen, S. J. Su, T. L. Windus, M. Dupuis, and J. A. Montgomery, *J. Comput. Chem.* **14**, 1347 (1993).
- ⁷¹M. S. Gordon and M. W. Schmidt, in *Theory and Applications of Computational Chemistry: The First Forty Years*, edited by C. E. Dykstra, G. Frenking, K. S. Kim, and G. E. Scuseria (Elsevier, Amsterdam, 2005), p. 1167.
- ⁷²Y. Zhao and D. G. Truhlar, *Theor. Chem. Acc.* **120**, 215 (2008).
- ⁷³Y. Zhao and D. G. Truhlar, *Acc. Chem. Res.* **41**, 157 (2008).
- ⁷⁴T. H. Dunning, *J. Chem. Phys.* **90**, 1007 (1989).
- ⁷⁵D. E. Woon and T. H. Dunning, *J. Chem. Phys.* **98**, 1358 (1993).
- ⁷⁶T. H. Dunning, K. A. Peterson, and A. K. Wilson, *J. Chem. Phys.* **114**, 9244 (2001).
- ⁷⁷E. Papajak, J. Zheng, X. Xu, H. R. Leverentz, and D. G. Truhlar, *J. Chem. Theory Comput.* **7**, 3027 (2011).
- ⁷⁸A. D. Boese and N. C. Handy, *J. Chem. Phys.* **116**, 9559 (2002).
- ⁷⁹M. J. Frisch, G. W. Trucks, H. B. Schlegel, G. E. Scuseria, M. A. Robb, J. R. Cheeseman, G. Scalmani, V. Barone, B. Mennucci, G. A. Petersson, H. Nakatsuji, M. Caricato, X. Li, H. P. Hratchian, A. F. Izmaylov, J. Bloino, G. Zheng, J. L. Sonnenberg, M. Hada, M. Ehara, K. Toyota, R. Fukuda, J. Hasegawa, M. Ishida, T. Nakajima, Y. Honda, O. Kitao, H. Nakai, T. Vreven, J. A. Montgomery, Jr., J. E. Peralta, F. Ogliaro, M. Bearpark, J. J. Heyd, E. Brothers, K. N. Kudin, V. N. Staroverov, R. Kobayashi, J. Normand, K. Raghavachari, A. Rendell, J. C. Burant, S. S. Iyengar, J. Tomasi, M. Cossi, N. Rega, J. M. Millam, M. Klene, J. E. Knox, J. B. Cross, V. Bakken, C. Adamo, J. Jaramillo, R. Gomperts, R. E. Stratmann, O. Yazyev, A. J. Austin, R. Cammi, C. Pomelli, J. W. Ochterski, R. L. Martin, K. Morokuma, V. G. Zakrzewski, G. A. Voth, P. Salvador, J. J. Dannenberg, S. Dapprich, A. D. Daniels, Ö. Farkas, J. B. Foresman, J. V. Ortiz, J. Cioslowski, and D. J. Fox, GAUSSIAN 09, Revision D.01, Gaussian, Inc., Wallingford, CT, 2009.
- ⁸⁰W. H. Press, S. A. Teukolsky, W. T. Vetterling, and B. P. Flannery, *Numerical Recipes in Fortran 77*, 2nd ed. (Cambridge University Press, 1992).
- ⁸¹J. Zheng, S. Zhang, B. J. Lynch, J. C. Corchado, Y.-Y. Chuang, P. L. Fast, W.-P. Hu, Y.-P. Liu, G. C. Lynch, K. A. Nguyen, C. F. Jackels, A. Fernandez Ramos, B. A. Ellingson, V. S. Melissas, J. Villà, I. Rossi, E. L. Coitino, J. Pu, T. V. Albu, R. Steckler, B. C. Garrett, A. D. Isaacson, and D. G. Truhlar, POLYRATE—version 2010-A, University of Minnesota, Minneapolis, 2010, <http://comp.chem.umn.edu/polyrate> (accessed June 14, 2016).
- ⁸²J. Zheng, Z.-H. Li, A. W. Jasper, D. A. Bonhommeau, R. Valero, R. Meana-Paneda, and D. G. Truhlar, ANT, version 2014-2, University of Minnesota, Minneapolis, 2015, <http://comp.chem.umn.edu/ant> (accessed June 14, 2016).
- ⁸³K. Kowalski and P. Piecuch, *J. Chem. Phys.* **120**, 1715 (2004).
- ⁸⁴K. Kowalski, *J. Chem. Phys.* **130**, 194110 (2009).
- ⁸⁵N. M. Zaripov, *J. Struct. Chem.* **17**, 640 (1976).
- ⁸⁶M. Nagasaka-Hoshino, T. Isozaki, T. Suzuki, T. Ichimura, and S. Kawauchi, *Chem. Phys. Lett.* **457**, 58 (2008).
- ⁸⁷M. Hoshino-Nagasaka, T. Suzuki, T. Ichimura, S. Kasahara, M. Baba, and S. Kawauchi, *Phys. Chem. Chem. Phys.* **12**, 13243 (2010).
- ⁸⁸M. Bossa, S. Morpurgo, and S. Stranges, *J. Mol. Struct.: THEOCHEM* **618**, 155 (2002).
- ⁸⁹I. F. Shishkov, L. V. Khristenko, N. M. Karasev, L. V. Vilkov, and H. Oberhammer, *J. Mol. Struct.* **873**, 137 (2008).
- ⁹⁰T. C. Allison, G. C. Lynch, D. G. Truhlar, and M. S. Gordon, *J. Phys. Chem.* **100**, 13575 (1996).
- ⁹¹D. G. Truhlar and C. A. Mead, *Phys. Rev. A* **68**, 032501 (2003).
- ⁹²O. Tishchenko, D. G. Truhlar, A. Ceulemans, and M. T. Nguyen, *J. Am. Chem. Soc.* **130**, 7000 (2008).